Effects of human sex chromosome dosage on spatial chromosome organization

Ziad Jowhar[a], Sigal Shachar[a], Prabhakar R. Gudla[b], Darawalee Wangsa[c], Erin Torres[d], Jill L. Russ[d], Gianluca Pegoraro[b], Thomas Ried[c], Armin Raznahan[d,*], and Tom Misteli[a,*]
[a]Cell Biology of Genomes Group, [b]High-Throughput Imaging Facility, [c]Genetics Branch, National Cancer Institute, and [d]Human Genetics Branch, National Institute of Mental Health, National Institutes of Health, Bethesda, MD 20892

ABSTRACT Sex chromosome aneuploidies (SCAs) are common genetic syndromes characterized by the presence of an aberrant number of X and Y chromosomes due to meiotic defects. These conditions impact the structure and function of diverse tissues, but the proximal effects of SCAs on genome organization are unknown. Here, to determine the consequences of SCAs on global genome organization, we have analyzed multiple architectural features of chromosome organization in a comprehensive set of primary cells from SCA patients with various ratios of X and Y chromosomes by use of imaging-based high-throughput chromosome territory mapping (HiCTMap). We find that X chromosome supernumeracy does not affect the size, volume, or nuclear position of the Y chromosome or an autosomal chromosome. In contrast, the active X chromosome undergoes architectural changes as a function of increasing X copy number as measured by a decrease in size and an increase in circularity, which is indicative of chromatin compaction. In Y chromosome supernumeracy, Y chromosome size is reduced suggesting higher chromatin condensation. The radial positioning of chromosomes is unaffected in SCA karyotypes. Taken together, these observations document changes in genome architecture in response to alterations in sex chromosome numbers and point to *trans*-effects of dosage compensation on chromosome organization.

INTRODUCTION

Sex chromosome aneuploidies (SCAs) are a class of genetic human syndromes that arise by the presence of an aberrant number of X and/or Y chromosomes beyond the typical XX for females and XY for males (Disteche, 2012). Commonly studied SCAs include Turner syndrome (X-monosomy in females [XO]) and Klinefelter syndrome, which arises due to the presence of a supernumerary X chromosome in males (XXY karyotype); other variations include XYY, XXX, and XXYY syndromes. These conditions are collectively common

(prevalence 2.5/1000) and associated with neurological, endocrine, immune, and metabolic phenotypes (Nielsen and Wohlert, 1991; Linden *et al.*, 1995; Bojesen *et al.*, 2003; Goswami *et al.*, 2003; Simpson *et al.*, 2003; Stochholm *et al.*, 2006; Chen *et al.*, 2012; Link *et al.*, 2013; Seminog *et al.*, 2015; Mankiw *et al.*, 2017). The downstream phenotypic consequences of SCAs presumably arise from the impact of atypical sex chromosome counts on genome function, but genomic features of SCA remain poorly understood in humans (Bermejo-Alvarez *et al.*, 2010; Arnold, 2012; Hughes and Rozen, 2012; Belling *et al.*, 2017).

To maintain cellular function, dosage compensation between males and females in mammals is normally achieved by silencing most of the genes in one of the two X chromosomes through a mechanism known as X chromosome inactivation (XCI), thus generating two functionally different X chromosomes, the inactive X (Xi) and active X (Xa; Clemson *et al.*, 1996; Avner and Heard, 2001). The initiation of XCI requires the noncoding Xist (X-inactive-specific transcript) RNA, a 17-kb-long untranslated transcript, which decorates Xi territories in *cis* (Brown *et al.*, 1991; Clemson *et al.*, 1996). Xist recruits various chromatin-modifying factors that induce heterochromatinization of the X chromosome, including histone methylation

(i.e., H3K27me3) and deacetylation (H4 hypoacetylation) via PRC1/2 and histone deacetylases (HDACs), respectively, repressive histones (macroH2A), and incorporation of DNA methylation (CpG islands) by various DNA methyltransferases (DNMTs; Plath *et al.*, 2002; de Napoles *et al.*, 2004; Chaumeil *et al.*, 2006; Engreitz *et al.*, 2013).

To date, few studies have directly examined X inactivation in tissues from humans with SCA. A recent microarray study of lymphoblastoid cell lines of a range of SCA karyotypes found that Xist activity increased sharply with increasing X-chromosome dosage, suggesting that the X-inactivation program is initiated for each additional X chromosome (Raznahan *et al.*, 2018). Furthermore, expression of X-linked genes that are known to escape X inactivation was positively correlated with X-chromosome dosage in SCAs, indicating that the phenomenon of escape is also maintained during inactivation of the supernumerary X chromosomes in SCA. However, the higher X-chromosome count across SCAs appears to be associated with a sublinear increase in expression of escapees, and a derepresssion of X-linked genes that are subject to X inactivation (i.e., expression greater in XO than XXX). Thus, current studies of gene expression in SCAs suggest that supernumerary X chromosomes are inactivated, but that additional regulatory mechanisms may be operating to shape expression from both the active X chromosome and the inactive X chromosome(s).

Given the presence of extra copies of sex chromosomes in SCAs, an unresolved question is whether the abnormal number of sex chromosomes leads to changes in the organization or spatial location of chromosomes within the nucleus. Chromosomes are spatially confined to discreet nuclear volumes, each referred to as chromosome territory (CT; Schardin *et al.*, 1985; Cremer *et al.*, 1993; Kurz *et al.*, 1996; Meaburn and Misteli, 2007) and they have characteristic, heterogeneous, but nonrandom distributions within the three-dimensional space of the nucleus (Borden and Manuelidis, 1988; Croft *et al.*, 1999; Bartova *et al.*, 2002; Parada *et al.*, 2004a,b; Misteli, 2007). Interestingly, the Xi forms a distinct, condensed and spherical structure (Barr body) and has a more peripheral position within the nucleus compared with the Xa chromosome (Chadwick and Willard, 2003; Bolzer *et al.*, 2005; Teller *et al.*, 2011).

In this study, we take advantage of a unique, comprehensive set of cells from individuals with various SCAs including XO, XXX, XXXX, XXY, XYY, XXYY, and XXXXY (Table 1) to probe the effects of sex chromosome supernumeracy on chromosome organization. Our studies are enabled by the recent development of HiCTMap, a 384-well plate–based chromosome paint fluorescence in situ hybridization (FISH) imaging method (Jowhar *et al.*, 2018) to characterize the size, shape, and positioning of chromosomes in large numbers of cells at high throughput. We find that in SCAs, the X chromosome undergoes architectural changes as a function of X copy number indicated by a decrease in size and increase in circularity, suggesting chromatin compaction. Similarly, the Y chromosome decreases in size as a function of Y copy number. All chromosomes studied maintain canonical spatial positioning regardless of sex chromosome number. Our results provide insight into the structural consequences of changes in genome organization induced by sex chromosome supernumeracy.

RESULTS
Detection and analysis of chromosome territories using HiCTMap in nuclei from SCA patients
To identify the effects of extra copies of either X and/or Y chromosomes on spatial genome organization, we applied the previously described high-throughput chromosome territory mapping (HiCTMap) method (Jowhar *et al.*, 2018). HiCTMap is a 384-well plate-

Karyotype	Set number	Sex	Age (yr)
XO	1	F	21
XX	1	F	22
XXX	1	F	14
XXXX	1	F	24
XXXXY	1	M	16
XXY	1	M	16
XXYY	1	M	21
XY	1	M	17
XYY	1	M	24
XO	2	F	13
XX	2	F	18
XXX	2	F	14
XXXX	2	F	11
XXXXY	2	M	13
XXY	2	M	19
XXYY	2	M	12
XY	2	M	8
XYY	2	M	21
XO	3	F	14
XX	3	F	17
XXX	3	F	16
XXXX	3	F	12
XXXXY	3	M	16
XXY	3	M	16
XXYY	3	M	13
XY	3	M	25
XYY	3	M	19

Description of patient-derived skin fibroblast cells used for experiments. Karyotypes, sex, and ages are indicated. Cells were obtained by skin punch biopsy.

TABLE 1: Primary skin fibroblast cells: description and origin.

based imaging method that allows systematic, high-resolution imaging of thousands of nuclei in hundreds of samples and it can accurately measure structural features of chromosomes such as size, shape, and spatial position at the single chromosome level (Jowhar *et al.*, 2018). We applied this pipeline to a comprehensive set of patient-derived primary cells that were acquired via skin biopsy from seven SCA patients (XO, XXX, XXXX, XXXXY, XXY, XXYY, XYY) and normal male (XY) and female (XX) controls (Figure 1A and Table 1). Skin fibroblast cells from three patients per karyotype that ranged from ages 8 to 25 were analyzed (Table 1). Cells were routinely cultured for no more than three to seven passages before analysis to minimize the possibility of genomic changes and their stable karyotype was confirmed by spectral karyotyping (SKY; unpublished data). Normal cell growth was verified using the proliferation marker Ki-67 (Supplemental Figure S1) and normal cell cycle profiles were observed at various cell densities (Supplemental Figure S2). Chromosomes 18, X, and Y were routinely detected by HiCTMap in all cell lines (Figure 1, A and B). For image analysis, we used modified KNIME-based image analysis workflows
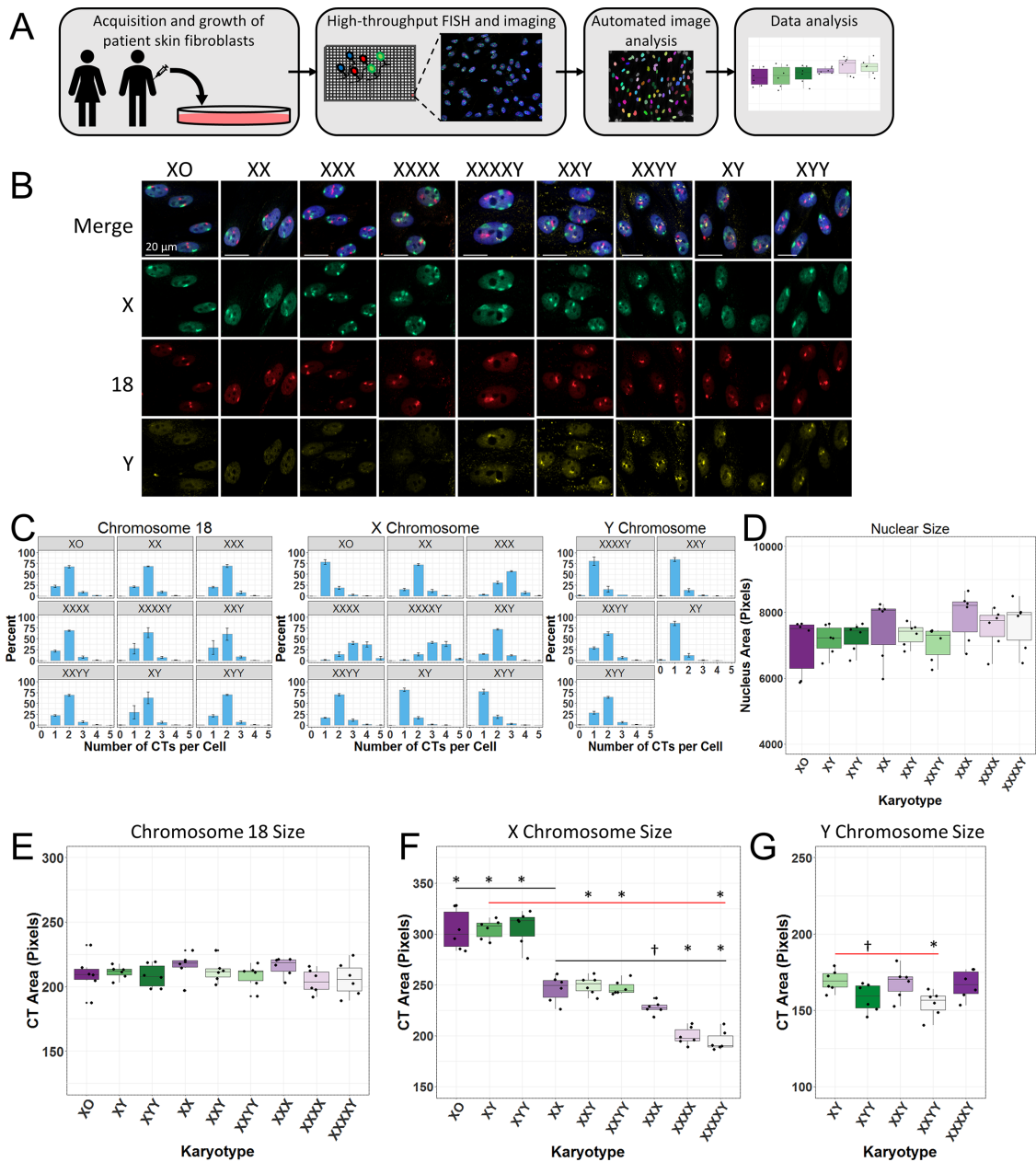
FIGURE 1: HiCTMap detection in SCA nuclei. (A) HiCTMap outline. Cells are acquired from patients via skin biopsy and expanded in cell culture. Cells are plated in 384-well imaging plates and DNA FISH is carried out using chromosome paints, followed by automated image acquisition using high-throughput microscopy. Image analysis by KNIME segments the nuclei, detects CTs in three channels, and measures chromosome position, size, and CT number. These features are then analyzed and plotted using the R software. (B) Representative maximal projections of CTs in a set of SCA skin fibroblasts. Cells are stained with DAPI (Blue-408) and chromosome paint probes X-Green (Alexa488), 18-Red (Dy505), Y-Red (Dy505), and Y-FarRed (Dy651). Scale bar: 20 μm. (C) Histograms showing the number of CTs detected per nucleus in SCA and normal male and female cells. Bars represent the mean of three biological replicates; each replicate contains ~1500 cells analyzed per karyotype. (D) Nuclear area of all karyotypes. (E–G) CT area of chromosomes 18 (E), X (F), and Y (G). Boxes represent the 25th, 50th (median), and 75th percentiles of the distributions, and whiskers extend to 1.5× the interquantile range. Each dot represents a replicate that contained ~1,000 nuclei per karyotype. The red bar compares normal males to male SCA karyotypes. The black bar compares normal female to all karyotypes. (F) *: p value = 0.0001; †: p value = 0.07. (G) *: p value < 0.05; †: p value = 0.12. Statistics calculated using one-way ANOVA, and only significant differences are denoted.

(Ronneberger *et al.*, 2015; Gudla *et al.*, 2017; see *Materials and Methods*). These workflows extract various geometric and intensity-related features of the segmented CTs, including chromosome area and circularity, as well as their spatial position in the nucleus (Figure 1A). We typically analyzed a minimum of 1000 cells in at least three experimental replicates per karyotype per experiment.

We first sought to verify the aneuploidy status of the multiple karyotypes using HiCTMap. The number of X, Y, and as a control,

chromosome 18 CTs was determined for each karyotype. Chromosome 18 was selected as a control autosome because it is well characterized with regard to nuclear positioning (Croft *et al.*, 1999; Cremer *et al.*, 2003; Bolzer *et al.*, 2005). The control chromosome 18 was detected in two copies in 69% of cells when averaged across all karyotypes (Figure 1C). The expected number of X and Y chromosomes was detected in 40–80% of cells depending on karyotype (Figure 1C). As expected and previously described (Jowhar *et al.*, 2018), the number of individually distinguishable X chromosomes is lower in multi-X karyotypes (XXX, XXXX, XXXXY) than the actual number due to clustering of multiple homologue chromosomes that consequently appear as a single, enlarged CT (Jowhar *et al.*, 2018). Such clustering was observed in 20–60% of cells depending on karyotype with the extent of clustering correlating with the number of X chromosomes (Figure 1C). In these cases, the lack of proper CT segmentation was not caused by limitation of the image analysis segmentation algorithm because human visual inspection was equally unable to resolve the clustered chromosomes. For all further analyses, only nuclei that contained the expected number of chromosomes per karyotype were used.

Chromosome size upon increased X or Y copy number

The addition of extra copies of sex chromosomes could potentially lead to an increase in nuclear volume. To test whether nuclear size changes with an increasing amount of DNA in SCA karyotypes, we measured the mean nuclear area of all SCA karyotypes (see *Materials and Methods*). We find that the nuclear area of all SCA karyotypes does not show a statistically significant difference, irrespective of the number of X or Y chromosomes when compared with the corresponding normal XX or XY controls (one-way analysis of variance [ANOVA], p value > 0.05 for all comparisons; Figure 1D). Because nuclear size does not significantly change, we did not normalize CT size to nuclear area in further analyses.

We next measured the CT size of the control autosome 18 and sex chromosomes X and Y in all karyotypes (Figure 1, E–G). We find that the median area of autosome 18 is similar between different karyotypes with no statistically significant difference between karyotypes when compared with their corresponding normal control karyotypes XX or XY (p value > 0.05; Figure 1E; mean ± SD, range of XXXX = 204 ± 9 to XX = 217 ± 10; p value > 0.05). In contrast, the range of the median X chromosome area decreased with increasing X chromosome copy number (Figure 1F) from 313 ± 18 pixels in XYY to 190 ± 10 in XXXXY (p value < 0.05), as would be expected due to the compaction of inactivated X chromosomes. The median CT area was increased by ~25% between monosomy X karyotypes (XO, XY, XYY) and normal XX females (p value = 0.0001). In tetrasomy X karyotypes (XXXX, XXXXY), the median CT area decreases by 20 and 35% compared with XX or XY, respectively (p value = 0.0001; Figure 1F). These changes in mean X chromosome area with increasing X copy numbers are in line with the expectation of X inactivation of any supernumerary X chromosomes.

The median area of the Y chromosome did not differ between single Y karyotypes compared with normal XY (p value > 0.9). However, unexpectedly, we see a decrease in median Y CT area in XXYY and in XYY cells compared with XY (XY vs. XXYY: p value = 0.02; XY vs. XYY: p value = 0.12; Figure 1G). This decrease may be suggestive of a regulatory mechanism that compacts the Y chromosome to compensate for the increase in gene expression.

X-chromosome inactivation status in nuclei from SCA patients

It is well established that in cells from normal XX females, one X chromosome undergoes inactivation, and it is expected that with increasing X chromosome copy numbers the number of Xi chromosomes should increase so that only one Xa is maintained in noncancerous polysomic X karyotypes (Lyon, 1961; Therman *et al.*, 1980; Sarto *et al.*, 1987). We expanded HiCTMap to combine DNA and RNA FISH to detect both X CT using chromosome paints and Xist RNA using RNA FISH probes (see *Materials and Methods*). Xa and Xi territories were clearly distinguishable based on colocalization of Xist transcripts on the Xi CT (Figure 2). We find that in nuclei from all karyotypes only one X CT remains active, whereas all other X CTs undergo inactivation as determined by Xist staining (Figure 2A). Generally, the number of Xist foci correlated better with the expected number of X chromosomes than the X CT itself, because Xist covers a small, compact area that is more easily resolved both visually and with computational methods. When comparing three patient cell lines with multi X karyotypes, we detected the correct number of Xist stained X chromosomes in a similar number of cells per karyotype, which is indicative of little interpatient variability (Figure 2B). Furthermore, the low variance in XIST focus count within each karyotype group indicated low cellular heterogeneity in X-inactivation status. No visible Xist foci were detected in monosomy X karyotypes (Supplemental Figure S3, A and B). For further analyses, only nuclei containing the expected number of Xist foci were included.

Changes in X chromosome size and shape with increasing X dosage

To determine whether the architecture of the X chromosome changes in SCAs, we measured structural features of X CT including size and shape of both Xa and Xi (Figure 3). As expected, we observe a statistically significant difference between the mean Xa and Xi area in all SCA karyotypes (Xa > Xi; two-way ANOVA; p < 0.05 for all comparisons). However, the difference in size between Xa and Xi decreased with increased X dosage (Figure 3A). This was due to a marked reduction in the median size of the Xa CT with increasing X dosage (mean ± SD; XX = 282 ± 20, XXX = 259 ± 8, XXXX = 229 ± 12, XXXXY = 222 ± 14, XXY = 277 ± 4, and XXYY = 276 ± 9 pixels; Figure 3A, red dots). In tetrasomy X karyotypes, the mean Xa CT size decreases by as much as 20–30% compared with XX or XY, respectively (p values = 0.0001). Similarly, the Xa of monosomy X karyotypes is larger than the Xa in XX cells by 12% (p value < 0.0022). The Xi chromosome also decreased in size with increasing X copy number, although to a smaller extent (XX = 214 ± 13, XXX = 211 ± 6, XXXX = 189 ± 10, XXXXY = 184 ± 11, in XXY = 225 ± 17, and XXYY = 224 ± 13 pixels; Figure 3A, blue dots). The size of Xi in XXXX and XXXXY was reduced by 12% and 15%, respectively, when compared with XX, representing the normal X karyotype and containing a single Xi (p value < 0.01). The size of Xi in disomy X karyotypes did not change significantly (p value > 0.05). Additionally, trisomy X exhibits a 1.5% decrease in mean Xi CT area compared with XX, but this difference was not statistically significant (p value > 0.05).

The observation of a marked change in size of X CT was based on measurements of the mean X CT size in a population of cells. To determine whether the extent of X CT size reduction per cell is different between different karyotypes, we measured the ratio between Xi and Xa size on a per-cell basis to determine whether in each individual cell, all X CTs are reduced to the same extent (Figure 3B). The median Xi/Xa ratio in normal XX cells ranged from 0.88 ± 0.06 in XX cells to XXXX = 0.98 ± 0.06 in XXXX cells, suggesting that the Xa is decreased more drastically with increasing X copy number than the Xi (Figure 3B). To verify, we plotted the size of Xa CT versus the size of Xi CT on a per-cell basis (Figure 3C) and find that in 69–77% of cells, Xa is larger than Xi (Figure 3C). These
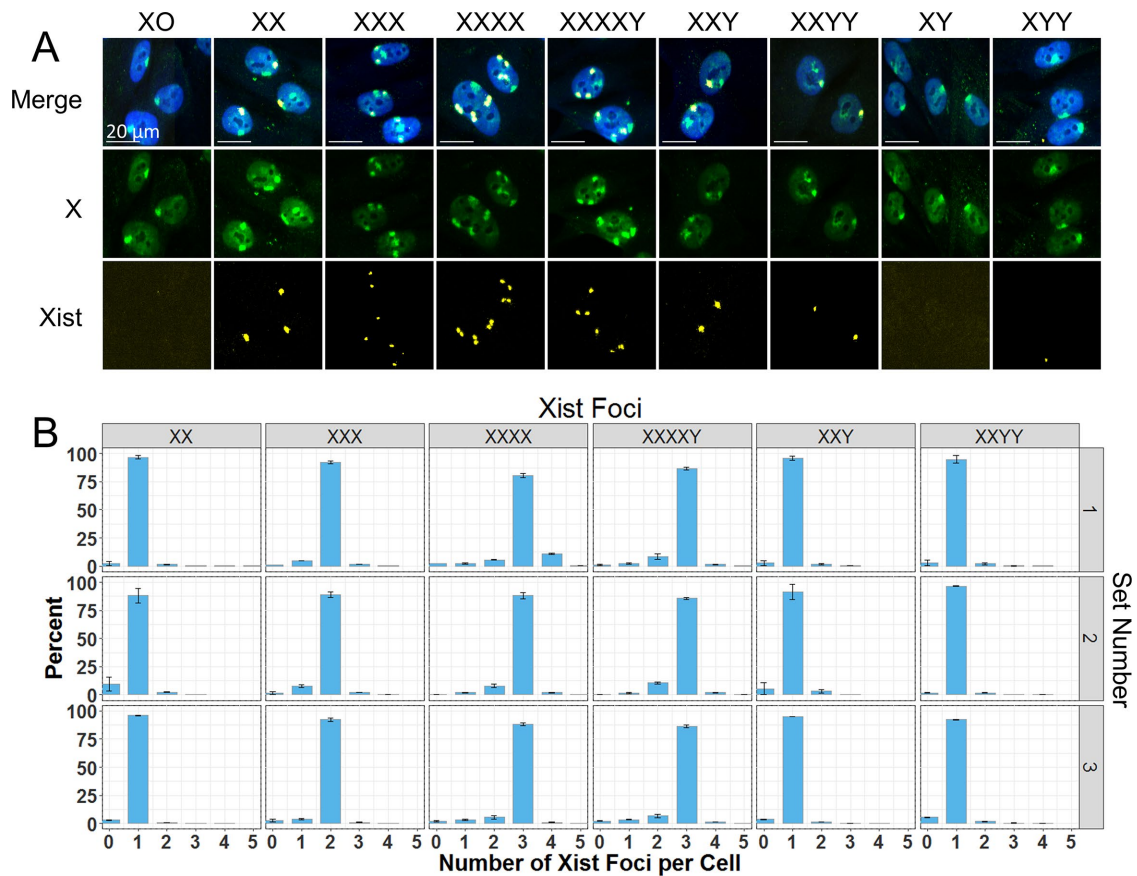
FIGURE 2: Xist RNA in SCA nuclei. (A) Representative maximal projection images of combined X chromosome DNA FISH and Xist RNA FISH. Cells are stained with DAPI (Blue-408) and X chromosome paint probes and Stellaris Xist Design Ready probe. Scale bar: 20 μm. (B) Number of Xist foci detected per nucleus in polyploid X nuclei. Error bars represent ± SD. Bars represent the mean between three biological replicates; each replicate contains approximately 1000 nuclei analyzed per karyotype.

observations demonstrate considerable variability in Xi and Xa size in individual cells and a size effect on both X chromosomes with increased X copy number.

Because we detected significant size changes in the X chromosome with increasing X copy number, we wanted to further characterize the structure of the Xa and Xi CTs in SCA karyotypes. We specifically measured the circularity of the chromosomes (defined as $(4\pi \text{ area})/(\text{perimeter}^2)$), as previous reports demonstrated that increased roundness or circularity of chromosomes is associated with compaction and heterochromatinization of the inactivated X chromosome (Bischoff *et al.*, 1993; Eils *et al.*, 1996; Clemson *et al.*, 2006; Teller *et al.*, 2011). As with size, the circularity of Xa chromosomes is X copy number dependent with an increase in mean Xa circularity from 0.57 ± 0.02 in XX to 0.61 ± 0.02 in XXXXY, and demonstrated a statistically significant difference when compared with XX or XY (p value < 0.005; Figure 3D, red dots). The mean Xi CT circularity, like size, increased from 0.67 ± 0.02 in XX to 0.7 ± 0.02 in XXXXY (p value < 0.02; Figure 3D, blue dots). This change in circularity is unique to the X chromosome as we do not see a change in the mean circularity of chromosomes 18 or Y (mean ± SD, 0.66 ± 0.02) in all SCA karyotypes with varying X copy number (Supplemental Figure S4). The circularity of chromosomes 18 and Y, which are both relatively small in size, gene poor, and compacted is comparable to the circularity of the Xi CT, which is transcriptionally inactive and highly compacted. In contrast, the circularity of the

transcriptionally active X chromosome is lower, suggesting that circularity measurements are a good estimate for the overall chromatin compaction state of chromosomes. Taken together, the increases in circularity observed for both the Xa and Xi with X copy number are suggestive of changes in the chromatin structure via an increase in heterochromatin in the presence of supernumerary X chromosomes.

Spatial positioning of chromosomes X, Y, and 18 in SCA nuclei

Owing to the nonrandom organization of the genome and observations that chromosome positioning may affect cellular function, we sought to test whether additional sex chromosomes affect the location of chromosomes X, Y, and 18 in the nucleus. Using HiCTMap as previously described (Jowhar *et al.*, 2018), we mapped the radial position relative to the center of the nucleus of CTs 18, X, and Y in all SCA karyotypes. For analysis, nuclei were divided into five equidistant shells, and the percentage of each CT in each shell was calculated (Croft *et al.*, 1999; Tanabe *et al.*, 2002; Bolzer *et al.*, 2005). We find that the radial position of chromosome 18 does not change between all SCA karyotypes with 12–24% of 18 CTs occupying each shell as shown previously in fibroblasts (Figure 4A; Bolzer *et al.*, 2005). As previously reported for XY, the Y chromosome was preferentially found in the interior of the nucleus with no significant difference between the various karyotypes (Figure 4B). The Y CT occupies
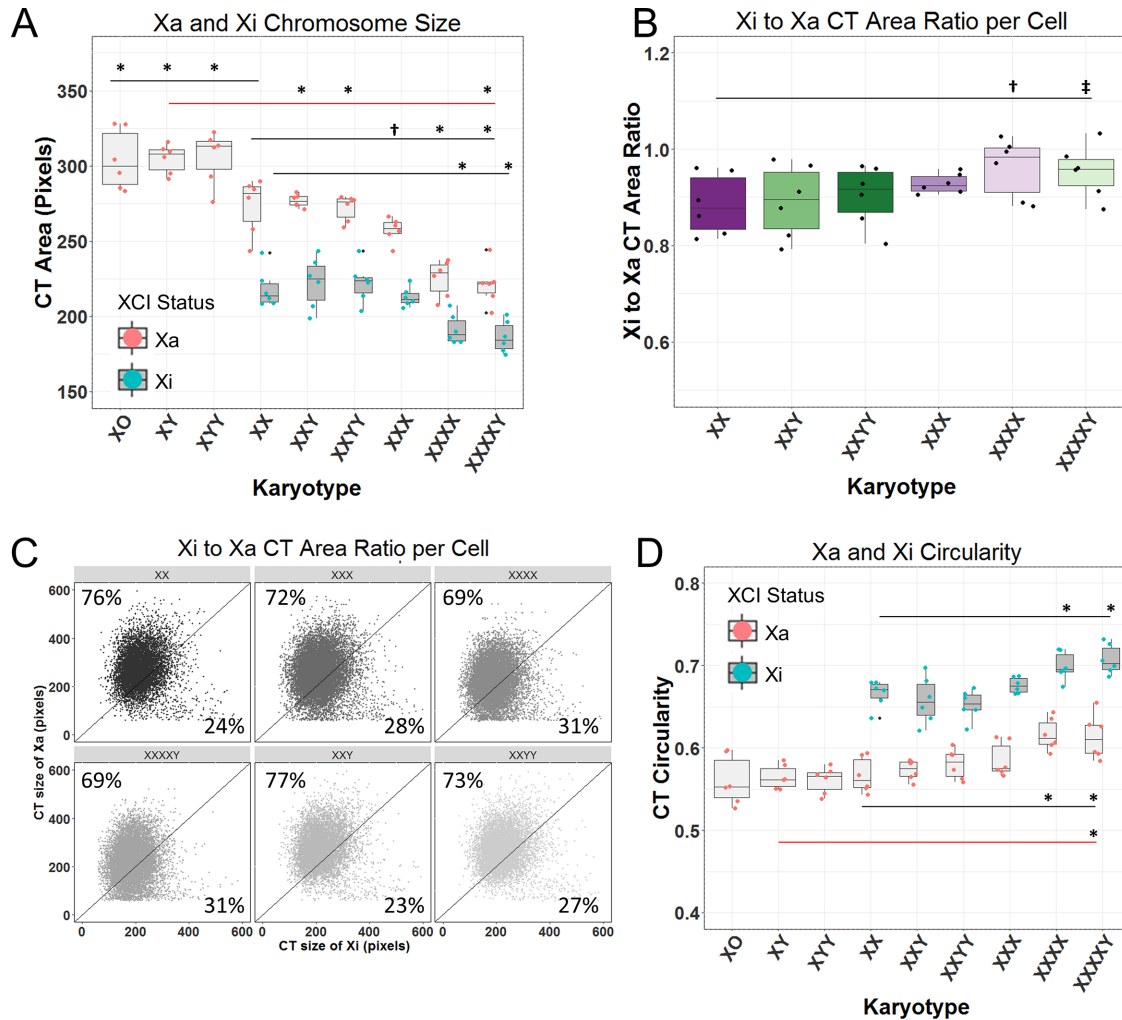
FIGURE 3: Chromosome Xa and Xi structural characterization in SCA nuclei. (A) CT area of Xa and Xi in SCAs and normal male and female nuclei. Red dots represent Xa CTs and blue dots represent Xi CTs. *: p value < 0.003. (B) Xi to Xa CT area ratio on a per-cell basis of polyploid X karyotypes. Each spot represents the mean of three replicates. †: p value = 0.12; ‡: p value = 0.19. (C) Xa CT area vs. Xi CT area on a per Xa basis of polyploid X karyotypes. Each dot represents a single Xa to Xi ratio in a single nucleus. Percentages represent the portion of ratios in which Xa is larger than Xi. (D) CT circularity of Xa and Xi in SCAs and normal male and female nuclei. Circularity is measured as $(4\pi$ area$)$/ perimeter^2. All box plots show the 25th, 50th (median), and 75th percentiles of the distributions, and whiskers extend up to 1.5× of the interquantile range. Each dot represents a replicate each containing ~1000 nuclei per karyotype. *: p value < 0.05. The red bar compares normal males to male SCA karyotypes. The black bar compares normal female to all karyotypes. Statistics calculated using one-way ANOVA, and only significant differences are denoted.

shells 3 and 4 with the highest percentage in all male SCA karyotypes (Figure 4B).

The X chromosome shows a strong peripheral positioning, as reported previously (Figure 4C; Belmont et al., 1986; Nagele et al., 1999; Bolzer et al., 2005; Petrova et al., 2007). With increasing X copy number, the positioning of the entire population of X chromosome becomes slightly more peripheral, due to the presence of the additional Xi chromosomes, which tend to be more peripheral than the Xa in interphase cells (Figure 4C; Belmont et al., 1986; Puck and Johnson, 1996; Rego et al., 2008; Chen et al., 2016). When positioning is measured individually for the Xa or Xi, both chromosomes maintain a strong peripheral positioning, with Xi exhibiting a more peripheral location compared with Xa in all multi-X karyotypes with a concurrent loss of Xi in the interior (Figure 4D; p value < 0.05). We conclude that SCAs do not affect positioning of the Xa or Xi.

DISCUSSION

We have used HiCTMap, a high-throughput imaging pipeline for the structural characterization and mapping of chromosome positions, to probe the effect of sex chromosome aneuploidy on genome architecture. The ability to analyze a large number of cells by high-throughput imaging enabled us to quantitatively determine the structural features and radial position of chromosomes in a unique set of primary cell lines from 27 SCA patients representing distinct karyotypes.

We find that SCAs do not induce changes in the size of the nucleus or the size of autosomal chromosome 18. However, we find that sex chromosome Y shows a decrease in its chromosome size with an increase in Y copy number, but not with increased X copy number. Similarly, we see changes in sex chromosome X size with the increase in X copy number, but not Y copy number. While the latter observation is explained by the well-established X-inactivation
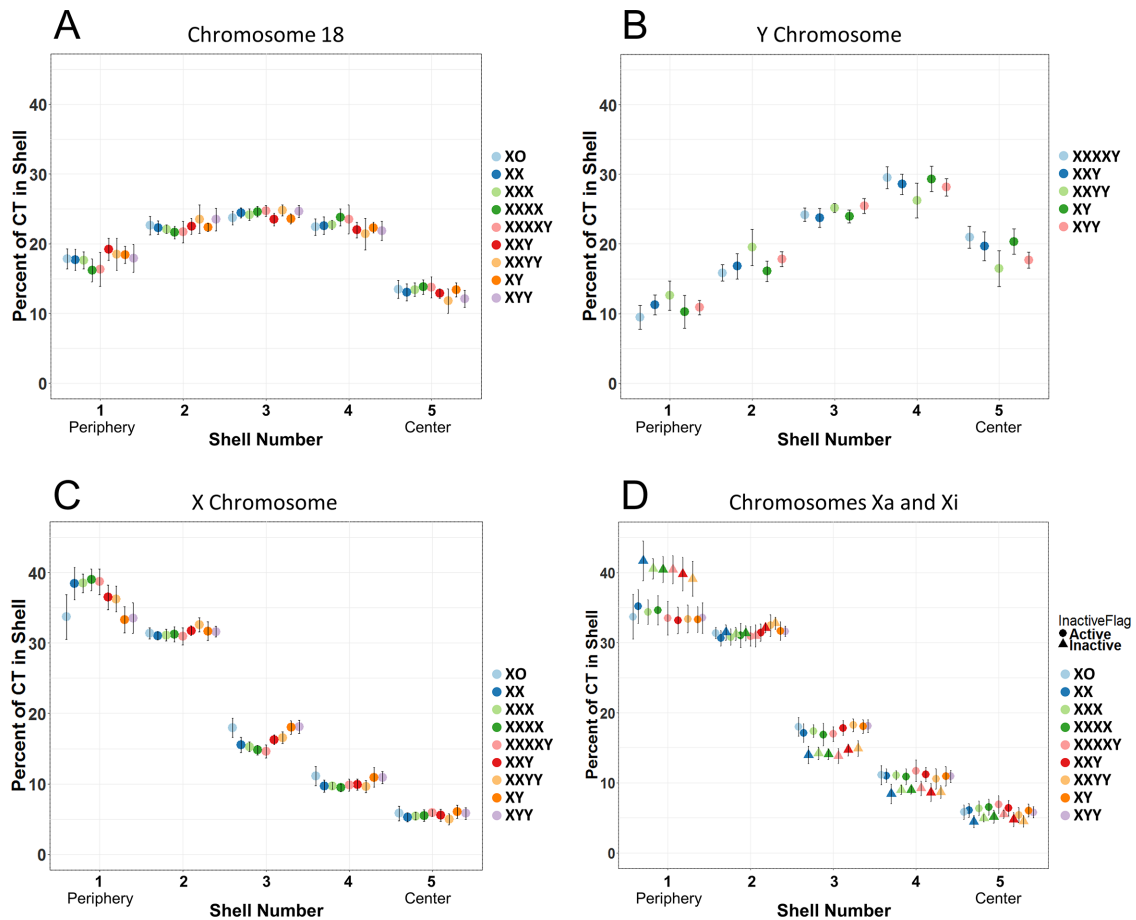
FIGURE 4: Radial positioning of chromosomes 18, X, and Y in SCA nuclei. (A) Distribution of the percentage of chromosome 18 in five concentric equidistant nuclear shells. Each spot represents the average of six replicates (three biological replicates, two experimental repeats each); each replicate contained ~1000 nuclei. (B) Distribution of the percentage of chromosome Y in five concentric equidistant nuclear shells. (C) Distribution of the percentage of chromosome X in five concentric equidistant nuclear shells. (D) Distribution of the percentage of chromosome Xa and Xi in five concentric equidistant nuclear shells. Triangles represent Xi CTs and circles represent Xa CTs. Error bars represent ± SD.

process used to compensate for the increased number of X chromosomes (Lyon, 1961; Boumil and Lee, 2001; Willard, 2014), the mechanism for the reduction of Y size is unknown. Chromosome Y is small, gene poor, and largely heterochromatic and the observed size change may be due to a mechanism by which cells attempt to compensate for the increase in gene dosage via changes in chromatin structure much like XCI, but to a lower extent. The effect on the Y chromosome is likely mediated by epigenetic mechanisms and may be necessary for maintaining cellular viability given the known capacity of some Y-linked genes, like SRY, to regulate the expression of autosomal and X-linked genes whose increased expression in the presence of multiple Y chromosomes may be harmful (Lemos *et al.*, 2008; Jiang *et al.*, 2010; Raznahan *et al.*, 2018).

Polysomic X SCA karyotypes have not been systematically and quantitatively studied by imaging and single cell analysis. Using a modified version of HiCTMap that combines RNA FISH and chromosome paint, we demonstrate that the XCI master regulator Xist is present on all supernumerary X chromosome(s) in polysomic X karyotypes in the vast majority of cells in the population. The presence of Xist is not affected by the number of Y chromosomes or an increase in Y copy number, for example, in XXYY cells.

Interestingly, we find changes in the size and shape of Xa and Xi in nuclei from different SCA karyotypes, indicative of changes in the overall level of chromatin compaction of the chromosome. We observe no difference in the size or circularity of Xa or Xi chromosomes as a function of Y copy number. In sharp contrast, the addition of X chromosomes leads to a marked decrease of 20–30% in size of the Xa chromosome with increased X copy number. The Xa chromosome is transcriptionally active and is the functional X chromosome in mammalian cells, but as more X chromosomes are introduced, Xa size decreases. This is in line with the observations that expression of X-linked genes has been found to be lower than expected based on the number of X chromosomes present in patients with increased X copy number. The increased X copy number does not solely involve silencing of genes from the additional inactive X chromosome, but also their further repression from the single active X chromosome by unknown mechanisms (Raznahan *et al.*, 2018). Compensating for the increase in X copy number, we find that the Xa chromosome is compacted and becomes similar in size to the Xi. Additionally, although less striking, any supernumerary Xi chromosomes also show a decrease in size with increasing X copy number, and approach a one to one ratio in size at a single cell level and population level (Figure 3, A and B). Also, we find increased chromosome compaction of the Xa and Xi, as measured by chromosome circularity, with increased X copy number. Chromosomes 18, Xi, and Y are smaller in all SCA karyotypes compared with the active

X chromosome. This is likely explained by the fact that chromosomes 18, Xi, and Y are largely heterochromatic, whereas the active X is more open and actively transcribed. Interestingly, we find that not only does the circularity of the Xi chromosome(s) increase with increased X copy number, but also that of the Xa chromosome, with an even higher rate than Xi chromosome(s). The structural changes in shape and size of the Xa and Xi point to a mechanism of global compaction by heterochromatinization of the X chromosome possibly as a way to regulate gene expression.

The reason why polysomic X SCA karyotypes are viable is most likely due to the inactivation of the supernumerary X chromosomes by XCI (Tsai *et al.*, 2009). In contrast, polysomy of chromosomes of similar size are often not viable probably due to the increased expression of the additional genes from the extra chromosomes (Tsai *et al.*, 2009; Rosenberg and Rosenberg, 2012). In addition, viable trisomies typically involve significantly smaller and gene poor chromosomes such as 18, 21, and Y (Pearson, 2001; Trump, 2010; Rosenberg and Rosenberg, 2012).

XCI is initiated by the spreading of Xist in *cis* across the future inactive X chromosome, which in turn recruits several proteins, such as lamin B receptor (LBR), polycomb repressive complex 1 (PRC1), and histone deacetylases (HDAC3), that initiate the transcriptional silencing and formation of a repressed nuclear compartment (Clemson *et al.*, 1996; Plath *et al.*, 2002; Chaumeil *et al.*, 2006; Zhao *et al.*, 2008; Pinheiro and Heard, 2017). As XCI is established and maintained, the Xi is enriched for repressive chromatin modifications including H2AK119Ub by PRC1, H3K27me3 by PRC2, DNA methylation, and incorporation of the histone variant macroH2A (Plath *et al.*, 2003; Silva *et al.*, 2003; Pinheiro and Heard, 2017). Upon full XCI, the Xi is transcriptionally repressed and tethered to the nuclear periphery via LBR and structurally compacted with escaped genes believed to be localized on the outside of the repressed compartment or the nucleolus (Avner and Heard, 2001; Plath *et al.*, 2002; Zhang *et al.*, 2007; Pinheiro and Heard, 2017). It is possible that, given the higher cellular levels of XIST in cells containing multiple Xis, Xist may sporadically associate with the Xa and induce chromatin alterations. This seems unlikely because we could not detect Xist staining bound to the Xa in polysomic X karyotypes. It seems more likely that the size reduction of Xa may be due to Xa heterochromatinization that is Xist independent. Prior observation of histone H4 acetylation in XXX, XXXXX, XXXXY, and XXXY karyotypes of the X chromosome showed alterations in deacetylation of histone H4 once the inactive state was established in polysomic X karyotypes (Leal *et al.*, 1998). In addition, demethylation of histone H4 lysine 20 to monomethyl by Dpy-21 is enhanced on the Xi chromosome in *Caenorhabditis elegans* (Brejc *et al.*, 2017). Furthermore, many of the genes that escape inactivation and are up-regulated in SCA karyotypes are chromatin remodelers and DNA methylases (Trolle *et al.*, 2016; Raznahan *et al.*, 2018), allowing for the possibility that as X copy number increases, repressive chromatin remodelers are deposited on the Xa chromosome, leading to the overall higher order structural changes we observe in the Xa and Xi chromosomes in SCA karyotypes.

Chromosomes are nonrandomly arranged in the mammalian cell nucleus (Dundr and Misteli, 2001; Parada and Misteli, 2002; Parada *et al.*, 2004a; Bickmore, 2013). We find no change in position of autosome 18 and sex chromosomes X and Y with increasing X or Y copy number. As previously demonstrated (Belmont *et al.*, 1986; Nagele *et al.*, 1999; Jowhar *et al.*, 2018) and in these experiments, the Y chromosome has a central position, whereas chromosome 18 is equally distributed across the nucleus in all SCA karyotypes. We observe a strong peripheral position of the X chromosome, which becomes stronger with increasing X copy number. However, when we distinguish the X chromosome by XCI status, we observe Xa is more internally positioned compared with Xi and does not show variability between karyotypes. Despite these differences, we observe that the Xa chromosomes of SCA karyotypes are similarly positioned, and the position of Xi chromosomes of SCA karyotypes, despite increasing Xi chromosomes, are unchanged. This suggests that regardless of X copy number, the previous observation of Xist mediated Xi tethering to the nuclear lamina is maintained (Chen *et al.*, 2016). Therefore, the spatial positioning of chromosomes remains consistent despite an increase in the number of sex chromosomes X or Y.

Taken together, while previous studies have focused on clinical and neurological implications of SCA, we have here probed the effects of supernumeracy of sex chromosomes on genome organization. Our findings document specific nuclear changes in chromosome size and structure, particularly of the X chromosome. These alterations may reflect changes in the global activity of the affected chromosomes, and it will be interesting to explore their relationship to gene dosage, most importantly of X-linked genes that may escape XCI, and in this way, contribute to the pathology of SCA diseases.

MATERIALS AND METHODS
Cell culture
Patient-derived primary skin fibroblasts (three of each karyotype: XO, XX, XXX, XXXX, XXXXY, XXY, XXYY, XY, and XYY) were grown in DMEM with 20% fetal bovine serum, 2 mM glutamax, and penicillin/streptomycin at 37°C and 5% CO_2. Cells were split 1:3 every 3–4 d and kept at a low passage (P3-9). Isolation and expansion of patient-derived primary skin fibroblasts was previously described (Jowhar *et al.*, 2018). Normal karyotype was verified by SKY. Patients were enrolled through a phenotypic characterization study of SCA at the National Institute of Mental Health (NIMH) Intramural Research Program. Informed consent and assent was attained from all participants and their parents: all study procedures were approved by a National Institutes of Health (NIH) Institutional Review Board.

High-throughput chromosome paint FISH in 384-well plates
High-throughput chromosome paint FISH was performed in triplicate wells as described (Jowhar *et al.*, 2018). Briefly, cells were plated in 384-well CellCarrier Ultra plates (Perkin-Elmer) at a concentration of 120 cells/µl (~3000 cells/well) and grown for 24 h. Cells were then fixed in 4% paraformaldehyde in phosphate-buffered saline (PBS) for 10 min, permeabilized in 0.5% Triton X-100/PBS for 20 min at room temperature (RT), and incubated in 0.1 N HCl for 10 min at RT. Cells were kept in 50% formamide/2× SSC (sodium chloride–sodium citrate buffer) for at least 30 min at RT.

Whole chromosome paint probes of human chromosomes 18, X, and Y were generated in house as previously described (Bischoff *et al.*, 1993; Macville *et al.*, 1997), and labeled using Spectrum Orange (Abbott Molecular), Dy505 (Dyomics), and Dy651 (Dyomics).

For hybridization, a probe mix solution containing 300 ng of each fluorescently labeled chromosome paint probe, 1 µg human COT1 DNA (Sigma-Aldrich Roche), and 30 µg salmon sperm DNA (Ambion) was ethanol precipitated and resuspended in 12 µl of hybridization buffer (20% dextran sulfate, 50% deionized formamide, 2× SSC, pH 7). The probe mix was then manually added to each well, denatured together with cells at 85°C for 7 min, and left to hybridize at 37°C overnight. Excess probe was washed three times with each: 2× SSC at 42°C, 1× SSC and 0.1× SSC at 60°C for 5 min. Cells were finally stained with 4′,6-diamidino-2-phenylindole (DAPI) in PBS (5 ng/µl) before imaging.

High-throughput chromosome paint and RNA FISH in 384-well plates

A DesignReady Xist RNA probe (Stellaris; 25 µM concentration) was diluted 1:10 in TE buffer, pH 8, and diluted again 1:17 in RNA hybridization buffer (10% formamide, 10% dextran sulfate in 2× SSC) to a final concentration of 150 nM. RNA probe (12 µl) in hybridization buffer was added to each well and plates were hybridized at 37°C in a humidified chamber for 4 h. Plates were then washed three times for 5 min with 2× SSC at 37°C. Cells were finally stained with DAPI in PBS (5 ng/µl) before imaging. After RNA FISH imaging, DNA FISH and imaging were completed sequentially as described above.

A subpixel, intensity-based image registration algorithm (Thevenaz et al., 1998) was used to align the maximum intensity projections of the RNA FISH and DNA FISH images. The DAPI channel from the two sequential acquisition sessions was used to estimate rigid body (translation and rotation) transformation, which was subsequently applied to the Xist RNA FISH image. The registration parameters were estimated for each field within a well using ImageJ's MultiStackRegistration plugin (version 1.46.2) embedded into KNIME image analysis workflow via the ImageJ Macro node.

High-throughput immunofluorescence in 384-well plates

Patient-derived skin fibroblasts were seeded in 384-well plates 24 h before fixation. Cells were fixed by the addition of paraformaldehyde to a final concentration of 4% for 10 min, washed once with PBS, permeabilized with PBS/0.5% Triton X-100 for 10 min, and then washed three times with PBS. Immunofluorescence staining was done by 1 h incubation with primary antibody diluted in block buffer (5% BSA/PBS), washed three times with PBS, 1 h incubation with fluorescently labeled secondary antibody and DAPI (2.5 µg/ml) diluted in block buffer (5% BSA/PBS), and washed three times with PBS. The following primary and secondary antibodies were used: mouse–anti-human Ki-67 (BD Transduction Laboratories;1:500) and Alexa Fluor rabbit–anti-mouse 488 (Invitrogen; 1:1000).

High-throughput cell cycle imaging

Cell cycle distribution was measured by high-throughput imaging as previously described (Roukos et al., 2015; Zane et al., 2017). Patient-derived skin fibroblasts were seeded in 384-well plates 24 h before fixation. Cells were fixed by the addition of paraformaldehyde to a final concentration of 4% for 10 min, washed once with PBS, permeabilized with PBS/0.5% Triton X-100 for 20 min, then washed three times with PBS. DNA was counterstained with 10 µg/ml DAPI for 10 min at RT and then washed three times with PBS. Cells were imaged using a 20× objective in epifluorescence using the Yokogawa CV7000 system. The analysis was conducted as described (Zane et al., 2017).

High-throughput image acquisition

Cells were imaged in four channels (405, 488, 561, and 640 nm excitation lasers) using the Yokogawa CV7000 confocal high-throughput imaging system with a 40× air objective lens (NA 0.95) and 16-bit sCMOS cameras and with no pixel binning. Image Z-stacks of 9–12 images at steps of 0.5 µm were acquired. Under these imaging conditions, the x-y pixel size was 162.5 nm and the field of view (FOV) size was 416 × 351 µm (2560 × 2160 pixels). At least 12–16 randomly sampled fields were imaged per well.

U-Net for segmenting nuclei and chromosome territories

The nucleus segmentation module from our previous work (Jowhar et al., 2018) was replaced with a fully convolutional neural network, FCN (Long et al., 2015).The FCN is based on U-Net architecture, a robust semantic segmentation model of detecting objects from biomedical images (Ronneberger et al., 2015). Briefly, the U-Net architecture is composed of an encoder and a decoder component with skip connections from encoder to decoder. We have previously used this architecture successfully for detecting spot-like structures (DNA FISH) in fluorescent images—SpotLearn (Gudla et al., 2017). The U-Net model for nucleus segmentation is identical to SpotLearn, except for the four spatial down-sampling layers in the encoder section of the network, as well as the four complementary spatial up-sampling (atrous deconvolution) layers in the decoder section. This modification results in a deeper model and more trainable parameters (7,759,521) than SpotLearn. The second column in the Supplemental Table ST1 describes relevant details about the U-Net model for nucleus segmentation. Since U-Net is a supervised, semantic segmentation model, it requires an input grayscale image and a corresponding binary mask of the objects in the grayscale image. So, to generate the training data for nucleus segmentation, we first selected the maximum intensity projections of the DAPI channel from 12 randomly selected FOVs (2560 × 2160 pixels) from an optimization plate. Next, the nuclei in these images were segmented using the seeded watershed and ultrametric contour map as described in our previous work (Jowhar et al., 2018). Then, we interactively merged all instances of oversegmented nuclei in the FOV into one object. The objects were merged using the "Interactive Label Editor" node in KNIME. Note that we did not correct for undersegmentation (i.e., overlapping or touching) of nuclei. The trained Random Forest classifier in our KNIME analysis workflow will filter these objects, based on nucleus morphology features. This strategy of using existing segmentation method(s) allowed us to rapidly generate binary masks for all DAPI stained nuclei in FOVs.

Before training the U-Net model for nucleus detection, we normalized the grayscale intensities of the DAPI channel to the bit-depth of the sCOMS camera(s) on the high-throughput microscope (16-bit, 65,536 intensity units). After normalization, we extracted 960 random patches of 256 × 256 pixels from the 12 FOVs of the DAPI channel and the corresponding binary mask. We allowed for overlapping windows during the patch extraction.

The U-Net model for nucleus detection was then trained on 864 (90% of 960) patches of 256 × 256 pixels, using modified Dice loss as described in the spot detection paper (Gudla et al., 2017), mini-batch ADAM optimizer, batch size of 1, initial learning rate of 1e-5, and maximum of 500 epochs. The model performance was evaluated after each epoch on 96 patches (10% of 960) by using the modified Dice loss between the ground truth and the model's prediction. The converged U-Net model for nucleus segmentation had a training and validation modified Dice loss of –0.99097 and –0.95865, respectively. During the inference stage for nucleus detection, the trained U-Net model was applied to the FOV of the DAPI channel (2560 × 2160 pixels) after normalizing the pixel values to the camera bit-depth (i.e., dividing each pixel intensity value by 65,535). The output generated by the U-Net model is the same size as the input image, but with each pixel value denoting the probability of belonging to the foreground (nucleus). The probability values in the output range from [0, 1] and we applied a hard threshold of 0.5 to convert pixels into nuclei class (pixel value > 0.5) or background class (pixel value ≤ 0.5). The foreground objects were then subjected to morphological operation for filling holes in the binary masks.

In this work, we also replaced the previously described methodology for CT segmentation (Jowhar et al., 2018)—the multiscale wavelet transform and Random Forest classifier responsible for filtering out false-positive CT detections—with a separate U-Net model. This U-Net model for CT segmentation is composed of only

three spatial down-sampling blocks in the encoder section of the network as well as three complementary spatial up-sampling blocks (atrous deconvolution) in the decoder section. The third column in Supplemental Table ST1 describes these details.

For generating the training data for the U-Net model for CT segmentation, we first applied the KNIME workflow for chromosome detection from our previous work on the images from an optimization plate (Jowhar *et al.*, 2018). Then, we manually selected, at random, a collection of 444 CT images, cropped to their nucleus binary mask, for which the CT segmentation mask(s) were visually accurate. The CT images, cropped to their nucleus binary mask, covered all combinations of chromosome X karyotypes, chromosome 18, or chromosome Y karyotypes that were used in this study.

These 444 grayscale images of CTs and their ground-truth binary masks were then centered and zero-padded to a uniform size of 128×128 pixels. After zero-padding, the intensity values of each CT image were rescaled to [0, 1] using the min-max normalization technique. We increased the training data to 888 by randomly rotating (90°, 180°, and 270°) the original set of 444 grayscale CT images and their corresponding binary masks.

The U-Net model for CT segmentation was then trained on 799 (90% of 888) grayscale CT images of 128×128 pixels using modified Dice loss (Gudla *et al.*, 2017), minibatch ADAM optimizer, batch size of 2, initial learning rate of 1e-5, and maximum of 3000 epochs with early stopping criteria. The model was evaluated after each epoch on 89 grayscale CT images (10% of 888) by using the modified Dice loss between the ground truth and the model's prediction. The converged U-Net model (epoch number 358) for detecting chromosome territories segmentation had a training and validation modified Dice loss of –0.96692 and –0.93595, respectively.

For inference on unseen CT images (cropped to the binary mask of the nucleus), we apply the min-max normalization of the intensity values in the CT grayscale image. Then, we center and zero-pad the normalized CT grayscale image. The centering and zero-padding to a uniform size allows one to use the U-Net model for CT segmentation to predict on large batches of nuclei (e.g., 256 nuclei). The exact number of nuclei in a batch that can be processed depends on the GPU memory and the complexity of the U-Net model.

The output generated by the U-Net model for CT segmentation has the same spatial dimensions as the input, but with pixel values denoting the probability of belonging to the foreground (chromosome territories). The probability values range from [0, 1], and we applied a hard threshold of 0.99 to convert pixels into CT class (pixel value ≥ 0.99) or background class (pixel value < 0.99). The binary masks of the foreground objects (CT class) were then labeled into individual objects using the connected-component labeling technique. Lastly, we discarded any CT object of less than 50 pixels for chromosomes X, Y, and 18, and of less than 5 pixels for RNA Xist.

Both the U-Net segmentation models were implemented in Python (version 2.7.12) using Keras frontend (version 2.0.5), Tensorflow backend (GPU version, 1.1.0), CUDA library (version 8.0), and cuDNN library (version 5.0). The bespoke Python scripts for training and inference were embedded into KNIME (64-bit, Linux, version 3.2.1) workflow(s) using the "Python Scripting" node. The training and inference of the U-Net model(s) were performed on Biowulf compute node(s) (High-Performance Computing Cluster, NIH) with Ubuntu 16.04 LTS (64-bit) and equipped with four Kepler 80 NVIDIA GPUs, each with 12 GB graphics memory.

Sample numbers and statistical analysis
Statistical analyses and graphics were generated using R version 3.3.2, 64-bit with the ggplot2 graphics package (version 2.2.1) and GraphPad Prism 7 version 7.01. *p* values were calculated using one-way ANOVA as indicated in the figure legends or two-way ANOVA, and *p* values of less than 0.05 were considered statistically significant. All comparisons of karyotypes were made to XX or XY, that is, XX versus XO, XXX, XXXX, XXXXY, XXY, XXYY, XY, XYY and XY versus XO, XXXXY, XXY, XXYY, XYY. Population values were calculated on a per karyotype and chromosome basis. Replicates were based on three patients, with each experiment containing three technical replicate wells performed in duplicate ($N = 6$). For each graph, a total of 18 wells were analyzed per karyotype. Approximately 1000 nuclei were analyzed per karyotype per experiment.

REFERENCES
Arnold AP (2012). The end of gonad-centric sex determination in mammals. Trends Genet 28, 55–61.

Avner P, Heard E (2001). X-chromosome inactivation: counting, choice and initiation. Nat Rev Genet 2, 59–67.

Bartova E, Kozubek S, Jirsova P, Kozubek M, Gajova H, Lukasova E, Skalnikova M, Ganova A, Koutna I, Hausmann M (2002). Nuclear structure and gene activity in human differentiated cells. J Struct Biol 139, 76–89.

Belling K, Russo F, Jensen AB, Dalgaard MD, Westergaard D, Rajpert-De Meyts E, Skakkebaek NE, Juul A, Brunak S (2017). Klinefelter syndrome comorbidities linked to increased X chromosome gene dosage and altered protein interactome activity. Hum Mol Genet 26, 1219–1229.

Belmont AS, Bignone F, Ts'o PO (1986). The relative intranuclear positions of Barr bodies in XXX non-transformed human fibroblasts. Exp Cell Res 165, 165–179.

Bermejo-Alvarez P, Rizos D, Rath D, Lonergan P, Gutierrez-Adan A (2010). Sex determines the expression level of one third of the actively expressed genes in bovine blastocysts. Proc Natl Acad Sci USA 107, 3394–3399.

Bickmore WA (2013). The spatial organization of the human genome. Annu Rev Genomics Hum Genet 14, 67–84.

Bischoff A, Albers J, Kharboush I, Stelzer E, Cremer T, Cremer C (1993). Differences of size and shape of active and inactive X-chromosome domains in human amniotic fluid cell nuclei. Microsc Res Tech 25, 68–77.

Bojesen A, Juul S, Gravholt CH (2003). Prenatal and postnatal prevalence of Klinefelter syndrome: a national registry study. J Clin Endocrinol Metab 88, 622–626.

Bolzer A, Kreth G, Solovei I, Koehler D, Saracoglu K, Fauth C, Muller S, Eils R, Cremer C, Speicher MR, Cremer T (2005). Three-dimensional maps of all chromosomes in human male fibroblast nuclei and prometaphase rosettes. PLoS Biol 3, e157.

Borden J, Manuelidis L (1988). Movement of the X chromosome in epilepsy. Science 242, 1687–1691.

Boumil RM, Lee JT (2001). Forty years of decoding the silence in X-chromosome inactivation. Hum Mol Genet 10, 2225–2232.

Brejc K, Bian Q, Uzawa S, Wheeler BS, Anderson EC, King DS, Kranzusch PJ, Preston CG, Meyer BJ (2017). Dynamic control of X chromosome conformation andr by a histone H4K20 demethylase. Cell 171, 85–102. e123.

Brown CJ, Ballabio A, Rupert JL, Lafreniere RG, Grompe M, Tonlorenzi R, Willard HF (1991). A gene from the region of the human X inactivation centre is expressed exclusively from the inactive X chromosome. Nature 349, 38–44.

Chadwick BP, Willard HF (2003). Chromatin of the Barr body: histone and non-histone proteins associated with or excluded from the inactive X chromosome. Hum Mol Genet 12, 2167–2178.

Chaumeil J, Le Baccon P, Wutz A, Heard E (2006). A novel role for Xist RNA in the formation of a repressive nuclear compartment into which genes are recruited when silenced. Genes Dev 20, 2223–2237.

Chen CK, Blanco M, Jackson C, Aznauryan E, Ollikainen N, Surka C, Chow A, Cerase A, McDonel P, Guttman M (2016). Xist recruits the X chromosome to the nuclear lamina to enable chromosome-wide silencing. Science 354, 468–472.

Chen X, McClusky R, Chen J, Beaven SW, Tontonoz P, Arnold AP, Reue K (2012). The number of X chromosomes causes sex differences in adiposity in mice. PLoS Genet 8, e1002709.

Clemson CM, Hall LL, Byron M, McNeil J, Lawrence JB (2006). The X chromosome is organized into a gene-rich outer rim and an internal core containing silenced nongenic sequences. Proc Natl Acad Sci USA 103, 7688–7693.

Clemson CM, McNeil JA, Willard HF, Lawrence JB (1996). XIST RNA paints the inactive X chromosome at interphase: evidence for a novel RNA involved in nuclear/chromosome structure. J Cell Biol 132, 259–275.

Cremer M, Kupper K, Wagler B, Wizelman L, von Hase J, Weiland Y, Kreja L, Diebold J, Speicher MR, Cremer T (2003). Inheritance of gene density-related higher order chromatin arrangements in normal and tumor cell nuclei. J Cell Biol 162, 809–820.

Cremer T, Kurz A, Zirbel R, Dietzel S, Rinke B, Schrock E, Speicher MR, Mathieu U, Jauch A, Emmerich P, et al. (1993). Role of chromosome territories in the functional compartmentalization of the cell nucleus. Cold Spring Harb Symp Quant Biol 58, 777–792.

Croft JA, Bridger JM, Boyle S, Perry P, Teague P, Bickmore WA (1999). Differences in the localization and morphology of chromosomes in the human nucleus. J Cell Biol 145, 1119–1131.

de Napoles M, Mermoud JE, Wakao R, Tang YA, Endoh M, Appanah R, Nesterova TB, Silva J, Otte AP, Vidal M, et al. (2004). Polycomb group proteins Ring1A/B link ubiquitylation of histone H2A to heritable gene silencing and X inactivation. Dev Cell 7, 663–676.

Disteche CM (2012). Dosage compensation of the sex chromosomes. Annu Rev Genet 46, 537–560.

Dundr M, Misteli T (2001). Functional architecture in the cell nucleus. Biochem J 356, 297–310.

Eils R, Dietzel S, Bertin E, Schrock E, Speicher MR, Ried T, Robert-Nicoud M, Cremer C, Cremer T (1996). Three-dimensional reconstruction of painted human interphase chromosomes: active and inactive X chromosome territories have similar volumes but differ in shape and surface structure. J Cell Biol 135, 1427–1440.

Engreitz JM, Pandya-Jones A, McDonel P, Shishkin A, Sirokman K, Surka C, Kadri S, Xing J, Goren A, Lander ES, et al. (2013). The Xist lncRNA exploits three-dimensional genome architecture to spread across the X chromosome. Science 341, 1237973.

Goswami R, Goswami D, Kabra M, Gupta N, Dubey S, Dadhwal V (2003). Prevalence of the triple X syndrome in phenotypically normal women with premature ovarian failure and its association with autoimmune thyroid disorders. Fertil Steril 80, 1052–1054.

Gudla PR, Nakayama K, Pegoraro G, Misteli T (2017). SpotLearn: Convolutional neural network for detection of fluorescence in situ hybridization (FISH) signals in high-throughput imaging approaches. Cold Spring Harb Symp Quant Biol. 82, 57–70.

Hughes JF, Rozen S (2012). Genomics and genetics of human and primate y chromosomes. Annu Rev Genomics Hum Genet 13, 83–108.

Jiang PP, Hartl DL, Lemos B (2010). Y not a dead end: epistatic interactions between Y-linked regulatory polymorphisms and genetic background affect global gene expression in Drosophila melanogaster. Genetics 186, 109–118.

Jowhar Z, Gudla PR, Shachar S, Wangsa D, Russ JL, Pegoraro G, Ried T, Raznahan A, Misteli T (2018). HiCTMap: detection and analysis of chromosome territory structure and position by high-throughput imaging. Methods 142, 30–38.

Kurz A, Lampel S, Nickolenko JE, Bradl J, Benner A, Zirbel RM, Cremer T, Lichter P (1996). Active and inactive genes localize preferentially in the periphery of chromosome territories. J Cell Biol 135, 1195–1205.

Leal CA, Ayala-Madrigal ML, Figuera LE, Medina C (1998). Histone H4 acetylation analyses in patients with polysomy X: implications for the mechanism of X inactivation. Hum Genet 103, 29–33.

Lemos B, Araripe LO, Hartl DL (2008). Polymorphic Y chromosomes harbor cryptic variation with manifold functional consequences. Science 319, 91–93.

Linden MG, Bender BG, Robinson A (1995). Sex chromosome tetrasomy and pentasomy. Pediatrics 96, 672–682.

Link JC, Chen X, Arnold AP, Reue K (2013). Metabolic impact of sex chromosomes. Adipocyte 2, 74–79.

Long J, Shelhamer E, Darrell T (2015). Fully convolutional networks for semantic segmentation. Proc CVPR IEEE, 3431–3440.

Lyon MF (1961). Gene action in the X-chromosome of the mouse (Mus musculus L.). Nature 190, 372–373.

Macville M, Veldman T, Padilla-Nash H, Wangsa D, O'Brien P, Schrock E, Ried T (1997). Spectral karyotyping, a 24-colour FISH technique for the identification of chromosomal rearrangements. Histochem Cell Biol 108, 299–305.

Mankiw C, Park MTM, Reardon PK, Fish AM, Clasen LS, Greenstein D, Giedd JN, Blumenthal JD, Lerch JP, Chakravarty MM, Raznahan A (2017). Allometric analysis detects brain size-independent effects of sex and sex chromosome complement on human cerebellar organization. J Neurosci 37, 5221–5231.

Meaburn KJ, Misteli T (2007). Cell biology: chromosome territories. Nature 445, 379–781.

Misteli T (2007). Beyond the sequence: cellular organization of genome function. Cell 128, 787–800.

Nagele RG, Freeman T, McMorrow L, Thomson Z, Kitson-Wind K, Lee H (1999). Chromosomes exhibit preferential positioning in nuclei of quiescent human cells. J Cell Sci 112 (Pt 4), 525–535.

Nielsen J, Wohlert M (1991). Chromosome abnormalities found among 34,910 newborn children: results from a 13-year incidence study in Arhus, Denmark. Hum Genet 87, 81–83.

Parada L, Misteli T (2002). Chromosome positioning in the interphase nucleus. Trends Cell Biol 12, 425–432.

Parada LA, McQueen PG, Misteli T (2004a). Tissue-specific spatial organization of genomes. Genome Biol 5, R44.

Parada LA, Sotiriou S, Misteli T (2004b). Spatial genome organization. Exp Cell Res 296, 64–70.

Pearson PL. (2001). Trisomy A2—Brenner, Sydney. In: Encyclopedia of Genetics, ed. JH Miller, New York: Academic Press, 2056–2058.

Petrova NV, Yakutenko II, Alexeevski AV, Verbovoy VA, Razin SV, Iarovaia OV (2007). Changes in chromosome positioning may contribute to the development of diseases related to X-chromosome aneuploidy. J Cell Physiol 213, 278–283.

Pinheiro I, Heard E (2017). X chromosome inactivation: new players in the initiation of gene silencing. F1000Res 6 F1000 Faculty Rev-344.

Plath K, Fang J, Mlynarczyk-Evans SK, Cao R, Worringer KA, Wang H, de la Cruz CC, Otte AP, Panning B, Zhang Y (2003). Role of histone H3 lysine 27 methylation in X inactivation. Science 300, 131–135.

Plath K, Mlynarczyk-Evans S, Nusinow DA, Panning B (2002). Xist RNA and the mechanism of X chromosome inactivation. Annu Rev Genet 36, 233–278.

Puck TT, Johnson R (1996). DNA exposure and condensation in the X and 21 chromosomes. Stem Cells 14, 548–557.

Raznahan A, Parikshak NN, Chandran V, Blumenthal JD, Clasen LS, Alexander-Bloch AF, Zinn AR, Wangsa D, Wise J, Murphy DGM, et al. (2018). Sex-chromosome dosage effects on gene expression in humans. Proc Natl Acad Sci USA 115, 7398–7403.

Rego A, Sinclair PB, Tao W, Kireev I, Belmont AS (2008). The facultative heterochromatin of the inactive X chromosome has a distinctive condensed ultrastructure. J Cell Sci 121, 1119–1127.

Ronneberger O, Fischer P, Brox T (2015). U-Net: convolutional networks for biomedical image segmentation. Lect Notes Comput Sci 9351, 234–241.

Rosenberg LE, Rosenberg DD. (2012). Chromosome abnormalities. In: Human Genes and Genomes, San Diego: Academic Press, 141–167.

Roukos V, Pegoraro G, Voss TC, Misteli T (2015). Cell cycle staging of individual cells by fluorescence microscopy. Nat Protoc 10, 334–348.

Sarto GE, Otto PG, Kuhn EM, Therman E (1987). What causes the abnormal phenotype in a 49,XXXXY male? Hum Genet 76, 1–4.

Schardin M, Cremer T, Hager HD, Lang M (1985). Specific staining of human chromosomes in Chinese hamster x man hybrid cell lines demonstrates interphase chromosome territories. Hum Genet 71, 281–287.

Seminog OO, Seminog AB, Yeates D, Goldacre MJ (2015). Associations between Klinefelter's syndrome and autoimmune diseases: English national record linkage studies. Autoimmunity 48, 125–128.

Silva J, Mak W, Zvetkova I, Appanah R, Nesterova TB, Webster Z, Peters AH, Jenuwein T, Otte AP, Brockdorff N (2003). Establishment of histone h3 methylation on the inactive X chromosome requires transient recruitment of Eed-Enx1 polycomb group complexes. Dev Cell 4, 481–495.

Simpson JL, de la Cruz F, Swerdloff RS, Samango-Sprouse C, Skakkebaek NE, Graham JM Jr, Hassold T, Aylstock M, Meyer-Bahlburg HF, Willard HF, *et al.* (2003). Klinefelter syndrome: expanding the phenotype and identifying new research directions. Genet Med 5, 460–468.

Stochholm K, Juul S, Juel K, Naeraa RW, Gravholt CH (2006). Prevalence, incidence, diagnostic delay, and mortality in Turner syndrome. J Clin Endocrinol Metab 91, 3897–3902.

Tanabe H, Muller S, Neusser M, von Hase J, Calcagno E, Cremer M, Solovei I, Cremer C, Cremer T (2002). Evolutionary conservation of chromosome territory arrangements in cell nuclei from higher primates. Proc Natl Acad Sci USA 99, 4424–4429.

Teller K, Illner D, Thamm S, Casas-Delucchi CS, Versteeg R, Indemans M, Cremer T, Cremer M (2011). A top-down analysis of Xa- and Xi-territories reveals differences of higher order structure at ≥20 Mb genomic length scales. Nucleus 2, 465–477.

Therman E, Denniston C, Sarto GE, Ulber M (1980). X chromosome constitution and the human female phenotype. Hum Genet 54, 133–143.

Thevenaz P, Ruttimann UE, Unser M (1998). A pyramid approach to subpixel registration based on intensity. IEEE Trans Image Process 7, 27–41.

Trolle C, Nielsen MM, Skakkebaek A, Lamy P, Vang S, Hedegaard J, Nordentoft I, Orntoft TF, Pedersen JS, Gravholt CH (2016). Widespread DNA hypomethylation and differential gene expression in Turner syndrome. Sci Rep 6, 34220.

Trump D (2010). Clinical genetics. In: Basic Science in Obstetrics and Gynaecology, 4th ed., ed. C Williamson, London: Churchill Livingstone, 13–24.

Tsai AC-H, Pickler L, Tartaglia N, Hagerman R (2009). Chromosomal disorders and fragile X syndrome A2. In: Developmental-Behavioral Pediatrics, 4th ed., ed. WB Carey, AC Crocker, WL Coleman, ER Elias, and HM Feldman, Philadelphia: W.B. Saunders, 224–234.

Willard HF (2014). The sex chromosomes and X chromosome inactivation. In: The Online Metabolic and Molecular Bases of Inherited Disease, ed. AL Beaudet, B Vogelstein, KW Kinzler, SE Antonarakis, A Ballabio, KM Gibson, and G Mitchell, New York: The McGraw-Hill Companies, Inc.

Zane L, Chapus F, Pegoraro G, Misteli T (2017). HiHiMap: single-cell quantitation of histones and histone posttranslational modifications across the cell cycle by high-throughput imaging. Mol Biol Cell 28, 2290–2302.

Zhang LF, Huynh KD, Lee JT (2007). Perinucleolar targeting of the inactive X during S phase: evidence for a role in the maintenance of silencing. Cell 129, 693–706.

Zhao J, Sun BK, Erwin JA, Song JJ, Lee JT (2008). Polycomb proteins targeted by a short repeat RNA to the mouse X chromosome. Science 322, 750–756.